

# Dipolar Bose-Einstein condensates in triple-well potentials

Rüdiger Fortanier, Damir Zajec, Jörg Main and Günter Wunner

1. Institut für Theoretische Physik, Universität Stuttgart, 70550 Stuttgart, Germany

E-mail: ruediger.fortanier@itp1.uni-stuttgart.de,  
zajec@itp1.uni-stuttgart.de

**Abstract.** Dipolar Bose-Einstein condensates in triple-well potentials are well-suited model systems for periodic optical potentials with important contributions of the non-local and anisotropic dipole-dipole interaction, which show a variety of effects such as self-organisation and formation of patterns. We address here a macroscopic sample of dipolar bosons in the mean-field limit. This work is based on the Gross-Pitaevskii description of dipolar condensates in triple-well potentials by Peter *et al* 2012 J. Phys. B: At. Mol. Opt. Phys. **45** 225302. Our analysis goes beyond the calculation of ground states presented there and clarifies the role of excited and metastable states in such systems. In particular, we find the formation of phases originating from the interplay of several states with distinct stability properties. As some of the phases are formed by metastable states special attention is paid to the characteristics of phase transitions in real-time and the dynamical stabilisation of the condensate.

PACS numbers: 03.75.Lm, 05.65.+b, 67.85.-d

## 1. Introduction

One of the most interesting features of Bose-Einstein condensates (BECs) is the possibility of the investigation of quantum effects in a macroscopically controlled way. BECs have been experimentally realised with atoms sustaining a large magnetic dipole moment such as  $^{52}\text{Cr}$  [1–3] and, more recently,  $^{164}\text{Dy}$  [4, 5] and  $^{168}\text{Er}$  [6]. Very recently, fast progress towards the creation of BECs of polar molecules [7], which sustain large electric dipole moments, has been made. These developments have opened the field of research of effects generated by the dipole-dipole interaction (DDI). A major part of these effects can be summarised under the topics “self-organisation” and pattern formation. These effects are involved in the formation of a supersolid quantum phase. Menotti *et al* [8] have shown by calculations on the basis of the Bose-Hubbard model that the existence of a supersolid is closely connected to the appearance of metastable states in an optical lattice. However, the Bose-Hubbard description is only practicable for small atom numbers and cannot describe the collapse of the macroscopic wave function. The stability of these metastable states with respect to the collapse thus has to be analysed by the use of a method – like the mean-field description – which is able to describe the local divergence of the wave function’s amplitude.

A minimal system for the analysis of the effects mentioned above is a dipolar BEC in a triple-well (TW) potential. In Ref. [9] the Bose-Hubbard model was used to investigate the possible ground states for a mesoscopic sample of dipolar bosons up to 18 particles. There, four different ground-state phases have been observed. Peter *et al* [10] applied a mean-field approach to this system, yet, considering a macroscopic BEC. They found no clear separation of phases, and observed that some population distributions predicted by the Bose-Hubbard model are unstable within the Gross-Pitaevskii description. Most of these calculations were performed on a grid using imaginary-time evolution (ITE). While this is a globally convergent method for the linear Schrödinger equation, the ITE does not necessarily converge to the ground state in a nonlinear system such as the GPE. In Ref. [8] this fact has been used to find metastable states.

Dipolar BECs in double-well potentials have been investigated in [11, 12]. In this system three major phases have been found: In the first both wells are populated equally. The second is the symmetry-broken phase (macroscopic quantum self-trapping, MQST), in which the majority of the particles populates one well, and the third is the unstable phase, where the condensate wave function collapses. It has been pointed out in [12] and [13] that MQST is a dynamical effect arising from the interaction of the particles which reflects itself in the nonlinearity of the GPE.

In Ref. [14] Zhang *et al* have performed a mean-field three-mode approximation to dipolar BEC in triple-well potentials. They found that the inter-level coupling of the states changes depending on their inter-site interactions and leads to macroscopic phase transitions. Furthermore, they show that the long-range nature of the dipole-dipole interaction leads to new dynamical effects such as long-range Josephson oscillations, where tunnelling between the outer wells takes place with negligible alteration of the

population of the centre well.

Both approaches, the Bose-Hubbard model in Ref. [9] and the three-mode approximation in Ref. [14] cannot resolve the following answer which is crucial for a planned experiment: Are the states stable with respect to the collapse of the wave function when a macroscopic BEC is considered and therefore observable in an experiment?

This question can be answered by the use of the Gross-Pitaevskii equation as applied by Peter *et al* [10]. There, however, no excited states were calculated which we find playing a crucial role in the formation of phases and the dynamical behaviour of the condensate. The purpose of this paper is to show that these states, which sometimes exist simultaneously, are the reason for quantum phase transitions and can be used to detect such by its dynamical characteristics. In particular, we investigate a dipolar BEC in an external TW potential on the basis of the extended time-dependent GPE in the form

$$H\Psi(\mathbf{r}, t) = \left( -\frac{1}{2}\Delta + V_{\text{TW}} + V_{\text{dd}} + V_{\text{sc}} \right) \Psi(\mathbf{r}, t) = i\partial_t\Psi(\mathbf{r}, t), \quad (1)$$

with

$$\begin{aligned} V_{\text{TW}} &= -V_0 \sum_{i=1}^3 \exp\left( -\frac{2(x - q_x^i)^2}{\omega_x^2} - \frac{2y^2}{\omega_y^2} - \frac{2z^2}{\omega_z^2} \right), \\ V_{\text{dd}} &= 3Na_{\text{dd}} \int d^3r' \frac{1 - 3\cos^2\vartheta}{|\mathbf{r} - \mathbf{r}'|^3} |\Psi(\mathbf{r}', t)|^2, \\ V_{\text{sc}} &= 4\pi Na |\Psi(\mathbf{r}, t)|^2, \end{aligned}$$

where  $N$  is the number of particles and  $a_{\text{dd}}$  and  $a$  denote the dipole and scattering length, respectively. The centres of the three individual wells are given by  $q_x^1 = -l$ ,  $q_x^2 = 0$ , and  $q_x^3 = l$ . The dipoles are aligned along the  $z$ -axis, so that  $\vartheta$  is the angle between the  $z$ -axis and the vector  $\mathbf{r} - \mathbf{r}'$ . Here, we have adopted the unit system of Peter *et al* [10], which implies measuring all lengths in units of the inter-well spacing  $l$ , all energies in units of  $\hbar^2/ml^2$  and time in units of  $ml^2/\hbar$ , where  $m$  is the particle mass. The TW potential and the orientation of the dipoles is visualised in figure 1 for the repulsive configuration (the attractive configuration would imply the dipoles to be aligned in  $x$ -direction). The widths of the Gaussians for the external trap are chosen such that changing the polarisation direction does not change the on-site effects of the dipole interaction ( $\omega_x = \omega_z$ ) and that the stability of the condensate is higher than in the spherical case ( $\omega_y > \omega_{x,z}$ ). Furthermore,  $\omega_x$  has to be set to a value where the different wells are clearly distinct. We further assume the relevant time scale of the inter-well oscillations to be large in comparison with breathing-mode like oscillations. This corresponds to a sufficiently low tunnelling rate. The interesting effects mentioned above are expected to arise from the interplay between the short-range and the long-range nature of the interaction. We therefore included both kinds of interaction and assumed  $Na$  and  $Na_{\text{dd}}$  to be independently adjustable quantities, whereas the results do not explicitly depend on  $N$  due to the scaling properties of the GPE.

The paper is organised as follows. In section 2 we will briefly introduce the two

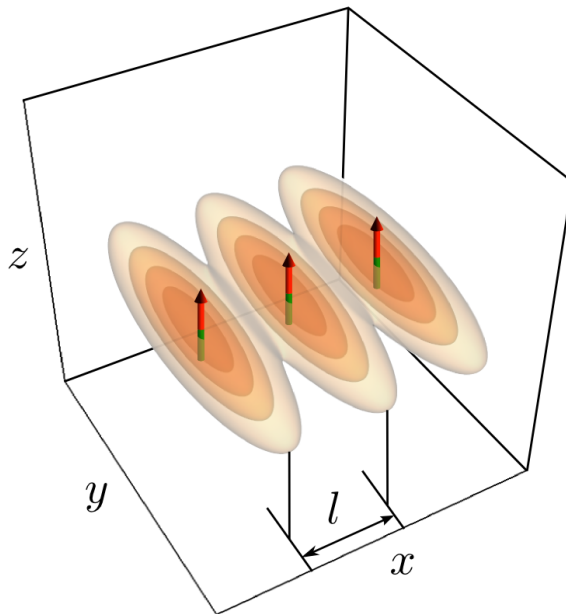


**Figure 1.** Visualisation of the TW potential. The dipoles are aligned in  $z$ -direction (repulsive configuration). The potential width  $L_y = \omega_y/2$  is 4 times larger than  $L_x$  and  $L_z$ . The parameter  $l$  denotes the distance between the minima of the potentials.

methods we used to solve the GPE. In section 3 we will present our results and investigate the system for two different sets of parameters in sections 3.1 and 3.2 in detail.

## 2. Methods

A well-known standard method to treat the dipolar GPE is the solution on a grid, and we use this technique for the computation of ground states and to simulate the real-time dynamics. However, the large number of grid points (and therefore parameters) does not allow us to obtain stationary states by a nonlinear root search. Thus, the accessibility of excited states, which do play a crucial role in the TW system, requires a larger effort, as it has been shown e.g. in [8, 15]. For this reason we also apply a variational approach with coupled Gaussian wave packets (GWPs) which has proven to be a full-fledged alternative to grid calculations [16–18] for the description of the ground and excited states as well as for real-time dynamics far beyond the stationary solutions.

### 2.1. Full-numerical grid calculations

The propagation of the macroscopic wave function  $\Psi$  in real time and the ITE for the calculation of stationary solutions can be performed on a grid. Particularly, ground states are calculated by the evolution of an initial wave function in imaginary time ( $t = -i\tau$ ) which dampens all other excited states.

For the linear Schrödinger equation the action of the time evolution operator  $U(\tau)$  on an initial state  $\psi$  can be investigated by expanding this state in the eigenfunctions  $\phi$  of the Hamiltonian  $H$

$$U(\tau) |\psi\rangle = e^{-H\tau} \sum_i |\phi_i\rangle \langle \phi_i | \psi \rangle = \sum_i e^{-E_i\tau} c_i |\phi_i\rangle. \quad (2)$$

Although the ITE dampens all of the eigenstates of the series, excited states vanish faster than the ground state. This guarantees the global convergence of the ITE. However, since in the nonlinear GPE the Hamiltonian depends on the actual state, the basis set of the expansion changes after each time step. Therefore the damping of the excited states cannot be assured. We thus have to compare the numerical results with the solution of the variational approach or choose an initial wave function which is sufficiently similar to the ground state. The latter can be realised by simply mapping the solution of the variational approach on the grid or by using previous numerical solutions with similar parameters. Even though we have not computed excited states by means of the ITE, such states can still be investigated on the grid when the solution of the variational approach is used as an initial wave function for dynamical simulations of the GPE.

We use the split-operator method for the grid calculations, where the scattering potential  $V_{\text{sc}}$  and the dipole-dipole potential  $V_{\text{dd}}$  have to be calculated at each time step. The latter can be evaluated by means of the convolution theorem. Altogether, we have to perform six Fourier transforms for each time step. A comprehensive presentation of this approach is given in [18].

## 2.2. Time-dependent variational approach

As an alternative to simulations on a grid the condensate wave function can be parametrised by a set of variational parameters, and the time evolution of the state is given by the time-dependence of the variational parameters. Our variational ansatz consists of a linear superposition of three GWPs. Each of the GWPs has the form

$$g^k = e^{-((\mathbf{x}^T - \mathbf{q}^k)^T A^k (\mathbf{x} - \mathbf{q}^k) - i(\mathbf{p}^k)^T (\mathbf{x} - \mathbf{q}^k) + \gamma^k)}, \quad (3)$$

where the symbol  $T$  denotes the transposition and where in general the time-dependent parameters  $A^k$  are  $3 \times 3$  complex symmetric matrices,  $\mathbf{p}^k$  and  $\mathbf{q}^k$  are real  $3d$  vectors, and  $\gamma^k$  are complex numbers. We assume that the  $z$ -direction (the direction of the dipole alignment) has a strong confinement due to the external trap and ignore translations and rotations in this direction by setting  $A_{xz}^k = A_{yz}^k = p_z^k = q_z^k = 0$ . However, for the other directions we apply no further restrictions, particularly with respect to position and movement of the GWPs in the  $x$ -direction. It is reasonable to start with one GWP placed at the centre of each well.

To determine the time-development of the variational parameters we make use of the time-dependent variational principle (TDVP) in the formulation of McLachlan [19]

$$I = \|\dot{i}\phi - H\Psi(t)\|^2 \stackrel{!}{=} \min, \quad (4)$$

where  $\phi$  is varied and set  $\phi \equiv \dot{\Psi}$  afterwards. The variational wave function

$$\Psi = \sum_{k=1}^3 g^k \quad (5)$$

is then inserted into (4) yielding the equations of motion (EOM) for the variational parameters

$$\dot{\mathbf{z}}^k = f(\mathbf{z}^k(t)) = f(A^k(t), \mathbf{q}^k(t), \mathbf{p}^k(t), \gamma^k(t)) . \quad (6)$$

Details can be found in [18], where the same method has been used to describe the collision of quasi-2d anisotropic solitons. Note that the method for the computation of the dipole integrals  $\langle V_{\text{dd}} \rangle$  in (1) slightly differs from the method used in [18]. In that work a strong confinement of the external trap is assumed in the  $y$ -direction perpendicular to the alignment of the dipoles, whereas here a strong confinement is assumed in the  $z$ -direction parallel to the alignment of the dipoles.

The stationary states are the fixed points of (6) and can be determined by a nonlinear root search (e.g. Newton-Raphson). An alternative to find the real ground state is the application of ITE to the EOM. However, as discussed in section 2.1 the ITE does not always converge to the ground state. In particular, if the initial wave function is close to that of an excited state, the ITE will stay for a rather long period in imaginary time on an plateau of almost the same mean-field energy. In practice, it is not always possible to distinguish between that case and the convergence to the ground state. To evolve the EOM in imaginary time as well as in real time, a standard algorithm like Runge-Kutta can be used. For a more detailed description see Ref. [18].

The linear stability of the fixed points can be investigated by the calculation of the eigenvalues  $\Lambda = \Lambda^r + i\Lambda^i$  of the Jacobian

$$J = \frac{\partial \left( \text{Re } \dot{A}^k, \text{Im } \dot{A}^k, \dot{\mathbf{q}}^k, \dot{\mathbf{p}}^k, \text{Re } \dot{\gamma}^k, \text{Im } \dot{\gamma}^k \right)}{\partial \left( \text{Re } A^j, \text{Im } A^j, \mathbf{q}^j, \mathbf{p}^j, \text{Re } \gamma^j, \text{Im } \gamma^j \right)} , \quad (7)$$

with  $k, j = 1 \dots 3$ . The eigenvalues appear in pairs of opposite sign and correspond to excitations described by the Bogoliubov-de Gennes equations [16, 17, 20]. If all real parts  $\Lambda^r = 0$ , the fixed point is stable, otherwise it is unstable.

### 3. Results

Placing the wells in the attractive configuration (dipole alignment  $\rightarrow\rightarrow\rightarrow$ ) enforces the atoms to occupy the centre well and does not show the same diversity of phases as the repulsive configuration ( $\uparrow\uparrow\uparrow$ ) does. We will therefore focus on the repulsive configuration, which is visualised in figure 1 and offers the possibility to investigate all effects of interest. For the TW potential  $V_{\text{TW}}$  in (1) the identical parameters  $V_0 = 80$  (this corresponds to  $\sim 16$  recoil energies [21]),  $\omega_x = \omega_z = 1/2$ , and  $\omega_y = 4$  as given in [10] have been used. Figure 2 shows the phase diagram for the repulsive configuration obtained by grid calculations.

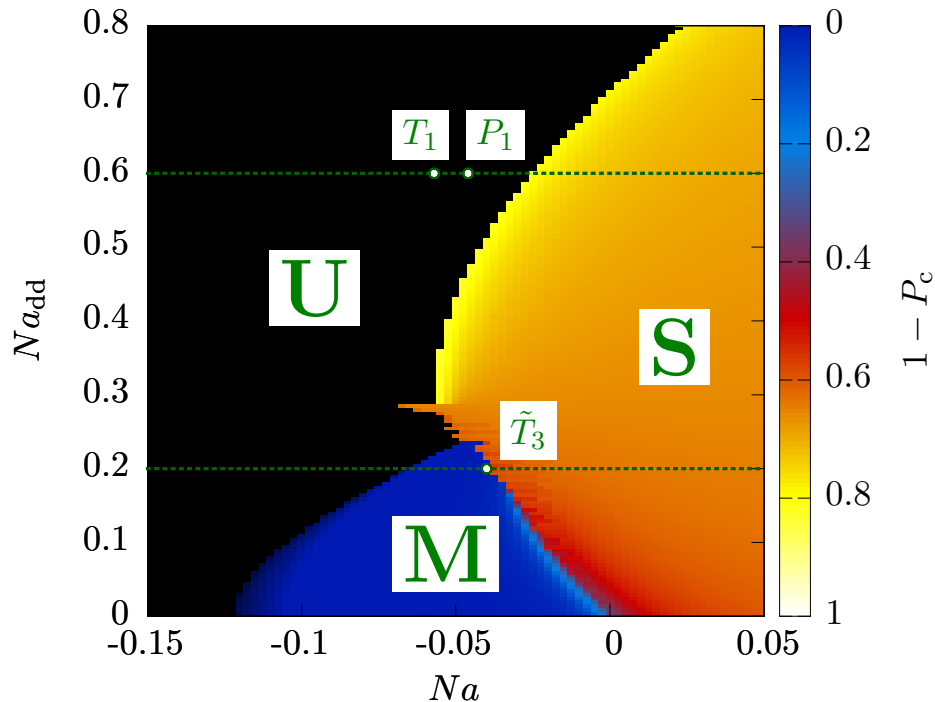


**Figure 2.** Phase diagram for the repulsive configuration. Coloured areas depict regions of parameter space where the ITE converges, whereas black areas indicate regions where the ITE does not converge. The colour bar represents the occupation of both outlying wells  $1 - P_c$ , where  $P_c$  is the population of the centre well. For details see the discussion in the text.

Our aim here is to understand the nature of the distinct regions and the mechanisms behind the phase transitions. The regions of the parameter space where the ITE converges are depicted in grey-scale (colour), whereas the black-coloured area U depicts the region where no convergence occurs. The grey-scale (colour) bar on the right-hand side shows the occupation of the two outlying wells with  $P_c$  being the occupation of the inner well. This means that the strip with  $1 - P_c \approx 0.8$  for dipole strengths  $Na_{dd} \gtrsim 0.3$  represents states where most of the particles are located in the outlying wells. Areas with  $1 - P_c \approx 2/3$  represent states where all three wells are equally occupied.

The phase diagram shows an interesting feature for  $Na_{dd} \lesssim 0.25$ : At some critical value of the scaled scattering length  $Na$ , the state, which the ITE converges to, exhibits a qualitative sudden change. Here the number of time steps until a given criterion for the convergence of the ITE is satisfied, reaches a local maximum. Below this critical scattering length we find an area in the phase diagram, marked as M, where  $1 - P_c \approx 0.1$  viz. almost all of the particles are located in the centre well. Decreasing the scattering length even more finally leads to the collapse of the condensate.

A similar result was presented by Peter *et al* [10]. The comparison with the phase diagram in [10], which has been calculated for the same set of parameters  $Na$  and  $Na_{dd}$ , shows the following differences regarding the convergence of the ITE. It does not show convergence of the ITE in the area M, whereas we do not find an additional white strip

( $1 - P_c \approx 1$ ) which should be located right next to the light (yellow) strip ( $1 - P_c \approx 0.8$ ) for values of  $Na_{\text{dd}} \gtrsim 0.3$ . This is not necessarily an inconsistency, but indicates the existence of metastable states in the system as will be discussed in detail in section 3.2.

For a better understanding of the phase diagram in figure 2 and in particular to clarify the nature of the phases U, S, and M and their transitions, we have performed two different vertical cuts at  $Na_{\text{dd}} = 0.6$  and  $Na_{\text{dd}} = 0.2$ , marked by the dashed horizontal lines. Along these lines, we calculated the stationary points by the use of the variational ansatz enabling us to investigate ground and excited states and their stability. In order to provide a deeper insight into the dynamical properties beyond the linear vicinity of the stationary states we subsequently performed real-time simulations.

### 3.1. Cut at $Na_{\text{dd}} = 0.6$

The results for  $Na_{\text{dd}} = 0.6$  are shown in figures 3 and 4. In figure 3 we immediately see that more than one state can be found. There are two tangent bifurcations  $T_1$  and  $T_2$  where two states emerge, respectively. We will denote these two pairs of states with  $S_1$  and  $S_2$ , and the symmetry-broken states bifurcating from  $S_2$  (see below) with  $S_{2\text{SB}}$ . If one investigates the linear stability by calculating the eigenvalues of the Jacobian in (7) one finds that at the tangent bifurcations all four born states are unstable. For the states born at  $T_2$  this stays true for all values of  $Na$ , but not for the states emerging at  $T_1$ .

In figure 4 the eigenvalues of the Jacobian are plotted for the  $S_2$ -state with the lower mean-field energy. It passes through a pitchfork bifurcation at  $P_1$  and becomes stable for higher values of  $Na$ . It can be seen as the stable ground state from there on. The point  $P_1$  is shifted to lower values compared to the border obtained by numerical grid calculations. However, the exact position of this border depends on the numerical method (e.g. the choice of initial conditions for the ITE; cf. [10]). Furthermore, the quantitative results of the variational solution is limited by the restrictions of the ansatz which uses only one GWP per well. We expect the variational results to converge with increasing number of GWPs [17]. In the bifurcation  $P_1$  two more states  $S_{2\text{SB}}$  are involved. The energies of these states are degenerate and the wave function breaks the symmetry of the trap (for one of them the left well is populated more than the right well, for the other one v.v.). The second state born in  $T_1$  also passes through a pitchfork bifurcation at  $P_2$  but becomes stable only in one of the eigenvalues while other unstable directions exist.

In figure 3c we plot the quantity  $I^k = \langle g^k | g^k \rangle$  which is a good estimate for the population of the  $k^{\text{th}}$  well, if we assume a small overlap of the GWPs. The states emerging at  $T_2$  show that the middle well is hardly populated. Nearly all particles are in the outer wells. We will call this a split-state. This is not the case for both of the states emerging at  $T_1$ , where (for the state with the lower mean-field energy) some particles are in the middle well. Note that the split-state is passing through such a symmetry-breaking pitchfork bifurcation at  $P_3$  as well. In fact, all states we investigated show this kind of symmetry-breaking behaviour, yet we did not analyse those in all cases.



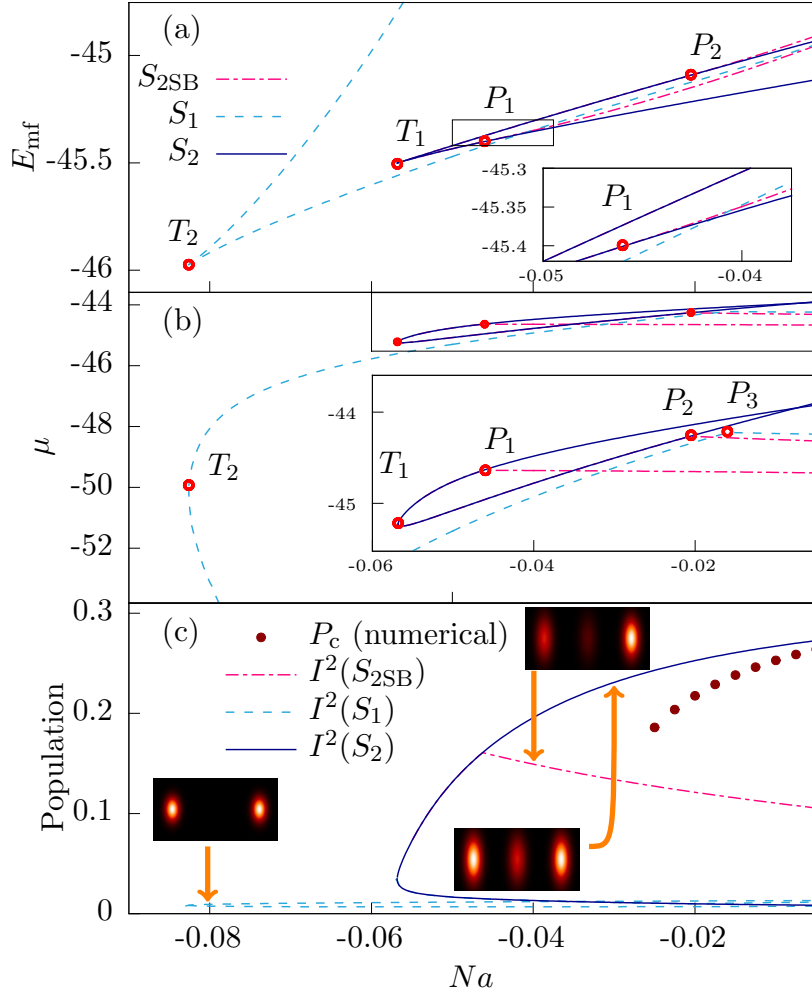


**Figure 3.** (a) Mean field energy and (b) chemical potential as functions of the scaled scattering length  $Na$  for dipolar interaction  $Na_{dd} = 0.6$ . The insets show magnifications of the rectangles. (c) Overlap integral  $I^2 = \langle g^2 | g^2 \rangle$  which shows the population of the centre well. All states shown in (a) are represented. The dots show the results of the grid calculations obtained by the ITE. The identically scaled absorption images show the qualitative shape of the wave function at the positions, where the arrows are pointing to.

An intriguing feature is the occurrence of a region between  $P_1$  and the crossing of the mean-field energy of the lower state of  $S_1$  and  $S_2$ , where we find an unstable state with a lower energy than the stable ground state (see inset in figure 3a). This is only possible due to the nonlinearity of the GPE. Nevertheless, it is interesting to perform real- and imaginary-time calculations in this region. It turns out that the ITE converges for a wide range of initial conditions to the stable ground state. However, if one starts close to the unstable state one finds a large plateau in the ITE, which is an indicator for the existence of metastable states.

The real-time evolution of the unstable states reveals that all of them have a small

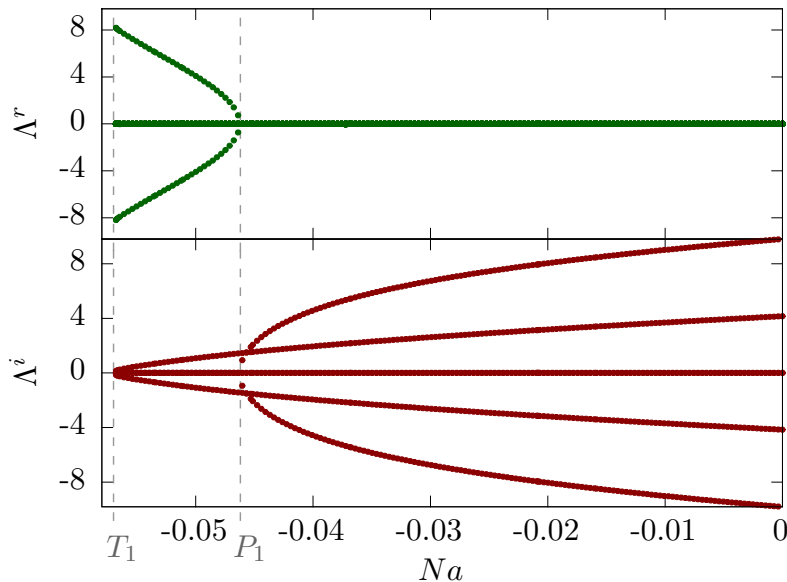


**Figure 4.** Eigenvalues  $\Lambda$  of the Jacobian (7) for the state  $S_2$  with the lower mean-field energy (see figure 3). The upper panel shows the real parts, the lower panel shows the imaginary parts. The state emerges unstable at the tangent bifurcation  $T_1$  which can be seen from the non-vanishing  $\Lambda^r$ . At the pitchfork bifurcation  $P_1$  the state becomes stable and can be viewed as the stable ground state from there on.

life time and mostly end in the collapse of the wave function. Calculations in which we decreased the scattering length as a function of time from the stable ground state to values of  $Na$  below  $P_1$  showed a similar behaviour. The dynamical properties become more complex at  $Na_{\text{dd}} = 0.2$  and will be discussed in more detail in section 3.2 where we will find a different scenario.

The results we have found provide a better understanding of the ITE-behaviour. In the calculation of the phase diagram in figure 2 for each  $Na$  the result of the ITE at the previous value of  $Na$  has been taken as the initial wave function. Obviously, this procedure gives rise to difficulties if crossings of states and metastable states are involved due to the small damping of states with almost the same energy as the ground state.

### 3.2. Cut at $Na_{\text{dd}} = 0.2$

We performed the second cut at  $Na_{\text{dd}} = 0.2$ . The results for the mean-field energy, chemical potential and the population of the centre well are shown in figure 5a-c, respectively. There are essentially three states  $\tilde{S}_1$ ,  $\tilde{S}_2$ , and  $\tilde{S}_0$  emerging in the tangent bifurcations  $\tilde{T}_1$ ,  $\tilde{T}_2$ , and  $\tilde{T}_3$ , respectively. The  $\tilde{S}_0$ -state with the lower mean-field energy born at  $\tilde{T}_3$  is the stable ground state. It is stable for the whole range of  $Na$ . The critical point where it becomes unstable therefore is given by the tangent bifurcation  $\tilde{T}_3$  (and not by any stability change in a pitchfork bifurcation, as for  $Na_{\text{dd}} = 0.6$  in figure 3). Furthermore, the energy of the ground state stays the lowest one for all  $Na$ , and no

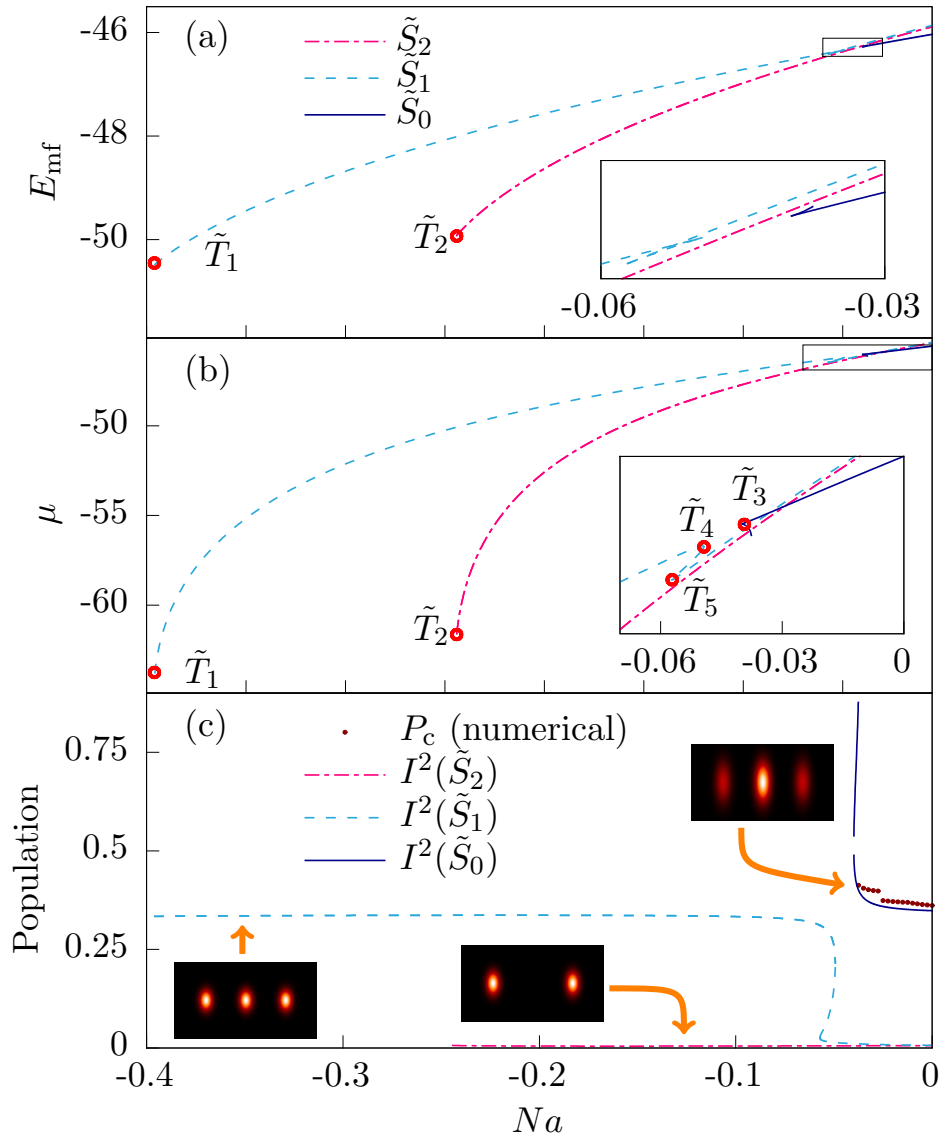


**Figure 5.** (a) Mean-field energy and (b) chemical potential as functions of the scaled scattering length  $Na$  for dipolar interaction  $Na_{\text{dd}} = 0.2$ . (c) Overlap integral  $I^2$  (c.f. figure 3) which shows the population of the centre well. The absorption images show the qualitative shape of the wave function at the positions, where the arrows are pointing to.

other state is crossing. The excited states emerging at  $\tilde{T}_1$  and  $\tilde{T}_2$  have been omitted for reasons of clarity. While  $\tilde{S}_2$  is a split-state for all  $Na$ ,  $\tilde{S}_1$  shows some interesting behaviour when it becomes energetically close to the ground state. It passes through two consecutive tangent bifurcations  $\tilde{T}_4$  and  $\tilde{T}_5$ . It can be seen in figure 5c that this involves a qualitative change of the wave function's nature from a state, where all wells are populated equally to a split-state.

It is a remarkable fact that we find (unstable) states for values of  $Na$  where in

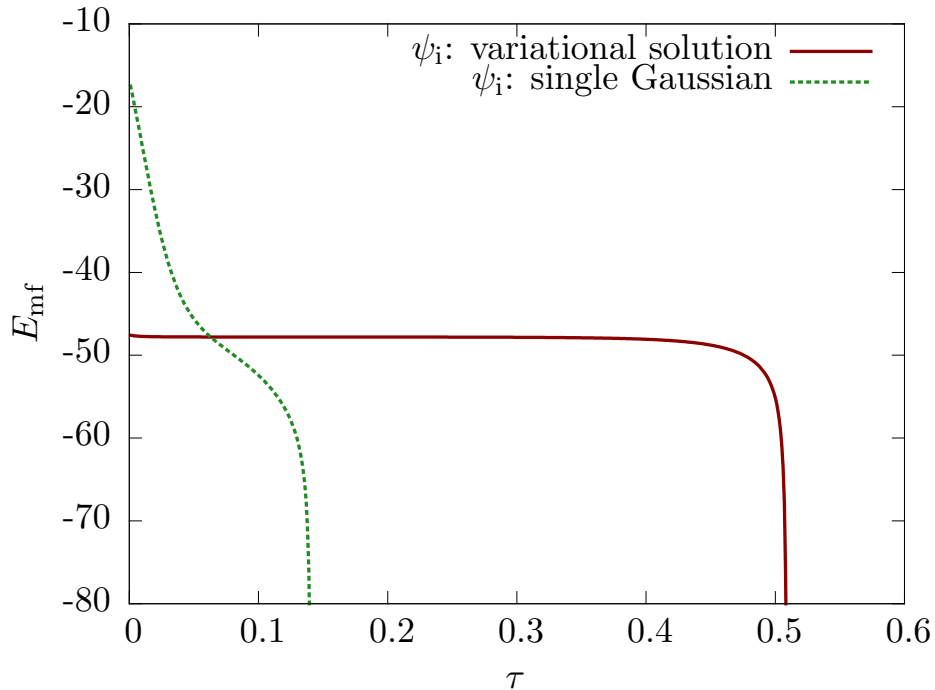


**Figure 6.** Mean-field energies as functions of imaginary time  $\tau$  for two grid-ITEs at  $Na_{\text{dd}} = 0.2$ ,  $Na = -0.2$ , where we have used as initial wave functions  $\psi_i$  a single Gaussian covering all wells for the calculation plotted as green dashed line and the variational solution of the state  $\tilde{S}_2$  plotted as red solid line.

figure 2 no ground state could be found, at all. More precisely, these states exist far below the critical scattering length at the tangent bifurcation  $\tilde{T}_3$ . This suggests a relation to the occurrence of regions in the parameter space such as the area M. The variational calculations predict that no stable ground state is present in the area M. Although the grid-ITE seems to converge in this area, this could still be just an effect of metastable states being present. This is illustrated in figure 6, where grid-ITEs with two different initial states  $\Psi_i$  are shown for  $Na = -0.2$ , which is in an area where no stable ground state exists. The closer the initial state to the metastable state is, the more pronounced the plateau in the ITE becomes. Finally, both calculations diverge, indicating that the state is unstable.

For a deeper insight into the physics of the metastable states we have investigated the dynamical properties in these regions. Real-time evolutions in which we change the scaled scattering length  $Na$  over time show that the dynamics of the condensate in this region of the parameter space differs from the dynamics in other regions.

Furthermore, the dynamical tuning of the scattering length can be a procedure in an experiment to access the metastable region. We illustrate this in figure 7a and b for the variational and grid calculations, respectively, where we have calculated the occupation of the centre well for two different real-time evolutions. The solid blue and dashed green curve represent the real-time evolutions for  $Na_{\text{dd}} = 0.2$  and an alteration of  $Na$  from  $-0.01$  to  $-0.03$  and from  $-0.03$  to  $-0.05$ , respectively. For the solid (blue)

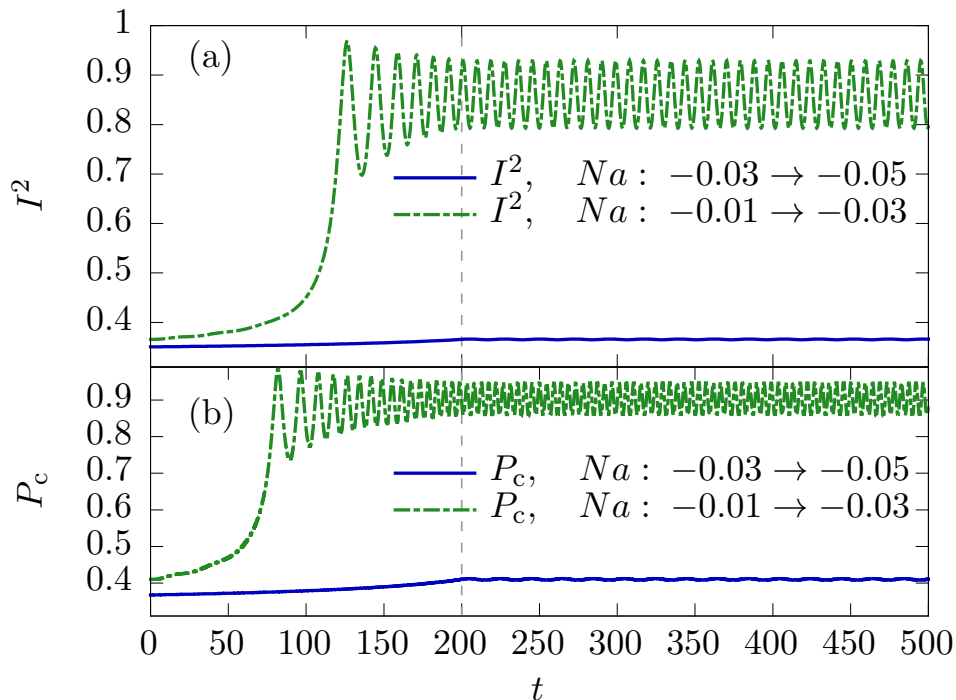


**Figure 7.** Real-time evolution for two transitions of  $Na$ . The scaled scattering length  $Na$  is tuned linearly from  $t = 0$  to its final value at  $t = 200$  and kept constant from there on. (a) Variational calculation with the overlap integral (introduced in figure 3c) of the middle well. (b) Population of the centre well obtained by the grid calculations is plotted as a function of time. In both panels (a) and (b) the solid blue line belongs to the calculation, where  $Na$  is tuned from  $-0.03$  to  $-0.05$  and the dashed green line belongs to the transition from  $Na = -0.01$  to  $Na = -0.03$ .

curve, the alteration of the scattering strength  $Na$  starts and ends in the region S (see figure 2) of the parameter space. This leads to small oscillations in the occupation of the centre well as soon as  $Na$  is adjusted to its final value at  $t = 200$ . For the dashed (green) curve small oscillations are visible as soon as we change the scattering length. Here, the alteration of  $Na$  ends in regions of the parameter space where the phase diagram given in [10] and the one presented in figure 2 differ. In this case, during the ramp-down of the scattering length the qualitative shape of the wave function changes significantly and large periodic oscillations set in. This indicates the phase transition from region S to M in figure 2. We conclude from these calculations that the metastable states can prevent the condensate from the collapse in some cases where no stable ground state exists.

In an experiment absorption imaging of the condensate during the ramp-down of the scattering length could reveal the phase transition. For an experimental setup we adopt the experimental parameters of Ref. [9] where a spacing of  $l = 1.7 \mu\text{m}$  is suggested. This setup can be realised by the use of  $^{52}\text{Cr}$  atoms where  $a_{\text{dd}} \sim 0.79 \text{ nm}$  and  $a \sim 5.8 \text{ nm}$ . The presented transition in parameter space would be equal to a number of 420  $^{52}\text{Cr}$  atoms where the scattering length would be tuned over a time of 475 ms via Feshbach resonances [22] to its final value. This alteration of the scattering length though can be

performed much faster, albeit with the consequence of enhanced oscillations in the centre well due to stronger excitations caused by the faster tuning of the scattering length.

If we use a single Gaussian function for the initial wave function of the ITE (dashed green line in figure 6), we observe a quick divergence of the wave function in imaginary time. Moreover, the real-time evolution of all states passed during this ITE yields an almost instant collapse of the condensate. However, if we choose a wave function from the plateau of the solid red line in figure 6 where the slope is minimal, we obtain a state where the real-time evolution does not yield an instant collapse, as it can be seen in figure 8. The variational calculation reveals that the corresponding state is metastable. From figure 5 we can see that no stable ground state exists for the set of parameters. The initial state has been calculated with high precision by the nonlinear root search. We therefore observe that the population of the wells stays constant for some time (see upper panel of figure 8). Then, a quasi-periodic symmetric oscillation sets in, where the population of the outer wells and the inner well is modulated periodically. After several oscillations the symmetry of this unstable oscillation is broken and chaotic oscillations between the wells set in.

In the grid calculations (see lower panel of figure 8) the population stays constant for a shorter time. This indicates that the metastable state is not perfectly hit (which is also visible by the slight symmetry-breaking of the initial state). Consequently, a complete break of the symmetry is reached earlier. The chaotic oscillations have a slightly higher frequency in the grid calculations. This is a consequence of the variational ansatz reducing the tunnelling between the wells.

The dynamics shown in figure 8 indicate that the unstable states contribute to the dynamical behaviour of the metastable states. In fact, we qualitatively find configurations where all wells are populated equally, split states, and symmetry-broken states during the real-time evolution of this metastable state.

#### 4. Conclusion

We studied the ground and metastable states of dipolar BECs in triple-well potentials both with a full-numerical ansatz and a time-dependent variational principle with coupled Gaussians. Although the triple-well potential constitutes a very simple system, the occurrence of different phases and their stability properties appears to be quite complicated. The phase diagram presented depicts a region of the parameter space, where multiple phases occur. This includes states where all wells are equally occupied as well as states where more particles are located in the centre or the both outer wells. The variational solutions reveal a variety of excited and unstable states including symmetry-broken states and unstable states in regions where no stable ground state exists. Real-time evolutions and the eigenvalues of the Jacobian  $J$ , given in (7), both allow for predictions about the stability of the investigated states. Moreover, the former is able to show whether the occupation of the wells for metastable states is characterised by quasi-periodic, chaotic oscillations, a break of symmetry, or whether the instability

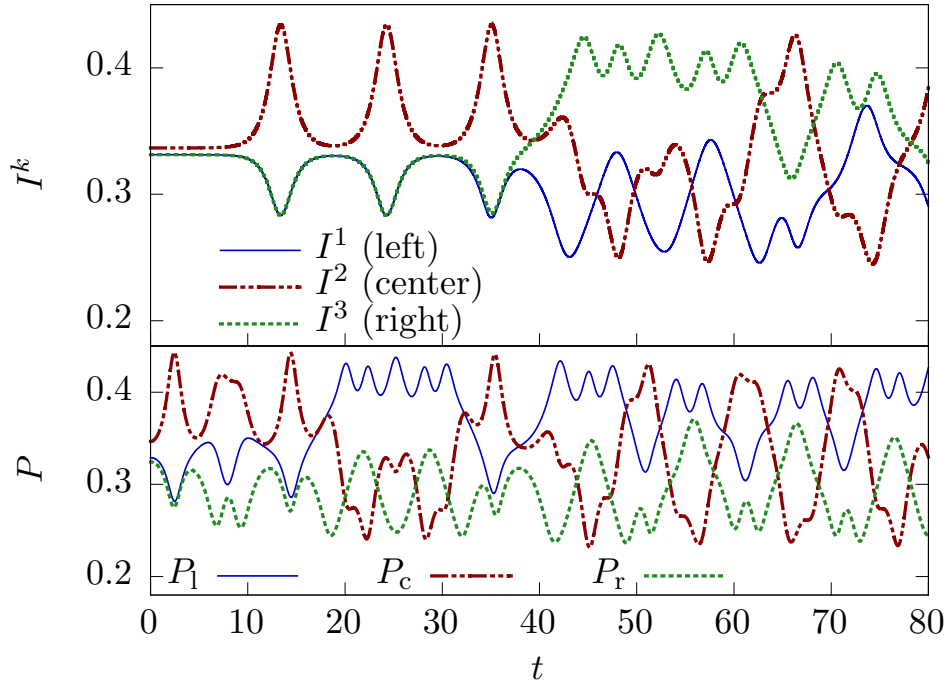


**Figure 8.** Real-time evolution of a metastable state for  $Na_{\text{dd}} = 0.2$  and  $Na = -0.2$ . The variational approach has been used for the calculation shown on the upper panel. The figure shows the overlap integrals  $I^k$  as already defined in figure 3. The lower panel shows the results of the grid calculation for the population  $P$  of the left, centre, and right well, respectively.

leads to a collapse. We have pointed out that a dynamical stabilisation of the condensate by the interplay of the metastable states is possible in those regions. Therefore, these regions are best candidates for the observation of a supersolid phase.

Further investigations should include multi-well potentials with additional wells and a different arrangement like a triangular or ring-like configuration. Our results should stimulate experimental efforts to study dipolar BECs in multi-well potentials.

## Acknowledgements

We thank David Peter and Tilman Pfau for valuable discussions. R.E. is grateful for support from the Landesgraduiertenförderung of the Land Baden-Württemberg. This work was supported by Deutsche Forschungsgemeinschaft.

## References

- [1] Griesmaier A, Werner J, Hensler S, Stuhler J and Pfau T 2005 *Phys. Rev. Lett.* **94** 160401
- [2] Beaufiles Q, Chicireanu R, Zanon T, Laburthe-Tolra B, Maréchal E, Vernac L, Keller J C and Gorceix O 2008 *Phys. Rev. A* **77** 061601(R)
- [3] T Lahaye, C Menotti, L Santos, M Lewenstein and T Pfau 2009 *Rep. Prog. Phys.* **72** 126401
- [4] Lu M, Youn S H and Lev B L 2010 *Phys. Rev. Lett.* **104** 063001

- [5] Lu M, Burdick N Q, Youn S H and Lev B L 2011 *Phys. Rev. Lett.* **107** 190401
- [6] Aikawa K, Frisch A, Mark M, Baier S, Rietzler A, Grimm R and Ferlaino F 2012 *Phys. Rev. Lett.* **108** 210401
- [7] Ni K K, Ospelkaus S, de Miranda M H G, Pe'er A, Neyenhuis B, Zirbel J J, Kotochigova S, Julienne P S, Jin D S and Ye J 2008 *Science* **332** 231–235
- [8] Menotti C, Trefzger C and Lewenstein M 2007 *Phys. Rev. Lett.* **98** 235301
- [9] Lahaye T, Pfau T and Santos L 2010 *Phys. Rev. Lett.* **104** 170404
- [10] Peter D, Pawłowski K, Pfau T and Rzażewski K 2012 *J. Phys. B: At. Mol. Opt. Phys.* **45** 225302
- [11] Xiong B, Gong J, Pu H, Bao W and Li B 2009 *Phys. Rev. A* **79** 013626
- [12] Asad-uz Zaman M and Blume D 2009 *Phys. Rev. A* **80** 053622
- [13] Raghavan S, Smerzi A, Fantoni S and Shenoy S R 1999 *Phys. Rev. A* **59** 620–633
- [14] Zhang A X and Xue J K 2012 *J. Phys. B: At. Mol. Opt. Phys.* **45** 145305
- [15] Rapedius K, Elsen C, Witthaut D, Wimberger S and Korsch H J 2010 *Phys. Rev. A* **82** 063601
- [16] Rau S, Main J and Wunner G 2010 *Phys. Rev. A* **82** 023610
- [17] Rau S, Main J, Cartarius H, Köberle P and Wunner G 2010 *Phys. Rev. A* **82** 023611
- [18] Eichler R, Zajec D, Köberle P, Main J and Wunner G 2012 *Phys. Rev. A* **86** 053611
- [19] McLachlan A D 1964 *Mol. Phys.* **8** 39–44
- [20] Kreibich M, Main J and Wunner G 2013 *J. Phys. B: At. Mol. Opt. Phys.* **46** 045302
- [21] Bloch I 2005 *Nat Phys* **1** 23–30 ISSN 1745-2473
- [22] Lahaye T, Koch T, Fröhlich B, Fattori M, Metz J, Griesmaier A, Giovanazzi S and Pfau T 2007 *Nature* **448** 672